Version of Record: https://www.sciencedirect.com/science/article/pii/S0376738823001308
Manuscript_0c4063c09f9f1358579fef6be1b652bd

Finely Tuning the Microporosity in Phosphoric Acid Doped Triptycene-Containing Polybenzimidazole Membranes for Highly Permselective Helium and Hydrogen Recovery

Yang Jiao [a,b], Mengdi Liu [c], Qi Wu [a,b], Peijun Zheng [d], Wei Xu [e], Bangjiao Ye [e], Hongjun Zhang [e], Ruilan Guo [c]* and Shuangjiang Luo [d]*

[a] *School of Rare Earths, University of Science and Technology of China, Hefei 230026, China*
[b] *Ganjiang Innovation Academy, Chinese Academy of Sciences, Ganzhou 341119, China*
[c] *Department of Chemical and Biomolecular Engineering, University of Notre Dame, Notre Dame, IN 46556, USA*
[d] *CAS Key Laboratory of Green Process and Engineering, State Key Laboratory of Multiphase Complex Systems, Beijing Key Laboratory of Ionic Liquids Clean Process, Institute of Process Engineering, Chinese Academy of Sciences (CAS), Beijing, 100190, China*
[e] *State Key Laboratory of Particle Detection and Electronics, University of Science and Technology of China, Hefei 230026, China*

Email: rguo@nd.edu (R. Guo), sjluo@ipe.ac.cn (S. Luo)

Abstract: High-performance polymer membranes with well-defined microporosity and size-sieving ability are especially attractive for helium and hydrogen recovery. Here we report novel macromolecular engineering of polybenzimidazole (PBI) membranes that integrate hierarchical triptycene units for high permeability and polyprotic acid doping for size sieving *via* controllable manipulation of microporous architecture. The triptycene moieties disrupt chain packing and introduce additional configurational free volumes, leading to significantly boosted He and H_2 permeabilities compared to previously reported PBI membranes. The acid doping resulted in crosslinked PBI membranes *via* hydrogen bonding and proton transfer with dramatically enhanced gas selectivities. Via adjusting the H_3PO_4-doping level, triptycene-based polybenzimidazole (TPBI) composite membranes (TPBI-$(H_3PO_4)_x$) exhibit the highest

© 2023 published by Elsevier. This manuscript is made available under the Elsevier user license
https://www.elsevier.com/open-access/userlicense/1.0/

gas selectivities for He enrichment (i.e., $\alpha(He/CH_4)$ = 7052 ± 156) and H_2 purification (i.e., $\alpha(H_2/CH_4)$ = 5128 ± 110) among existing polymeric gas separation membranes. Additionally, under mixed-gas conditions at 150 °C, the TPBI-$(H_3PO_4)_{0.98}$ membrane displays a H_2 permeability of 46.7 Barrer and a H_2/CO_2 selectivity of 16, far beyond the Robeson's 2008 upper bound for H_2/CO_2 separation. The facile and diverse tunability and excellent gas separation performance make TPBI-$(H_3PO_4)_x$ membranes highly attractive for helium and hydrogen separation.

Keywords: polybenzimidazole, gas separation membrane, triptycene, phosphoric acid doping, hydrogen recovery

1 Introduction

The fast-growing demand for clean and renewable energy has arisen to mitigate climate and environmental issues caused by carbon emissions. Hydrogen, produced mainly by steam reforming followed by the water-gas shift reaction, has emerged as a clean fuel and played increasingly essential roles in energy consumption (e.g., hydrogen fuel cell) if it can be purified efficiently from the shifted gas mixtures [1-6]. In addition, the unique characteristics of helium, which is currently extracted mostly from natural gas, render it indispensable in numerous critical medical and industrial applications [7]. However, the helium concentration in most natural gas reservoirs is rather low; thus, energy-efficient technologies of helium extraction are highly demanded. Membrane-based separations are believed to be promising in hydrogen and helium recovery as highly energy-efficient alternatives compared to conventional cryogenic distillation and pressure swing adsorption, ascribing to their continuous, easy, and low carbon footprint operation [8].

Process economics for membrane-based hydrogen and helium recovery favor high permeability and selectivity, and the latter is particularly critical to demanding purity requirements in the purification. The selectivities of H_2/CO_2 and He/CH_4 higher than 10 and 1000, respectively, can significantly reduce purification costs [9, 10]. Inorganic membranes, such as graphene oxide [11], zeolites [12], alumina [13], and metal-organic frameworks [14-16] were demonstrated to have high molecular-sieving ability for hydrogen and helium separations. However, it is a considerable challenge regarding the cost and quantity of production for commercial-scale use [8]. Polymeric membranes

have achieved industry-scale output for various gas separation applications (e.g., natural gas purification, air separation) and attracted substantial attention. However, due to the similar kinetic diameter of H_2 (2.9 Å) and CO_2 (3.3 Å) as well as more favorable CO_2-polymer interaction, commercial glassy polymer membranes usually displayed very low H_2/CO_2 selectivity (e.g., 2.5 for cellulose acetate, 2.4 for polysulfone, and 3.0 for Matrimid® polyimide [17]) due to the lack of well-defined microcavities that are crucial for molecular sieving.

Polybenzimidazole (PBI) is a family of aromatic heterocyclic polymers containing the imidazole ring structure. PBIs exhibit excellent thermal stability and molecular sieving properties when used as H_2/CO_2 separation membranes at elevated temperatures due to highly rigid backbone structure and strong intermolecular hydrogen bonding [18, 19]. However, existing commercial *m*-PBI membranes suffer from very low H_2 permeability. Various new diacids containing bulky groups, such as tetraaminodiphenylsulfone, isobutyl or trifluoromethyl groups, were employed to synthesize new PBI membranes with improved H_2 permeabilities [20-22] which, however, were always accompanied by compromised size sieving properties. Crosslinking has become an effective method to tighten polymer chain-packing for enhanced size sieving. For instance, the H_2/CO_2 selectivity of *m*-PBI went up to 140 after covalent crosslinking [23, 24]. The blend of *m*-PBI with Matrimid®5218 exhibited an H_2 permeability range of 0.6~27.1 Barrer with H_2/CO_2 selectivity up to 9.4 [25]. While highly selective, these low-free-volume PBIs still have less attractive gas permeabilities because of the lack of interconnected microcavities.

Recently, triptycene units were incorporated into polymer architecture for gas separation membranes, which showed superb performance [26-31]. Triptycene is constituted by benzene and isopropyl groups, which fuse into three-dimensional structures with characteristic configurational free volumes. Previous studies have demonstrated that incorporating triptycene moieties efficiently disrupts chain packing, leading to increased fractional free volume for high gas permeabilities. Additionally, the unique internal free volume between the benzene 'blades' has dimensions comparable to the kinetic diameters of common gases, which provides an excellent opportunity to increase gas permeability and size sieving simultaneously *via* optimizing the size and size distribution of free volume elements in corresponding polymers [26, 27, 32-35].

This study reports a series of novel triptycene-based PBIs with high gas permeabilities for hydrogen and helium recovery. Specifically, a new triptycene-based polybenzimidazole (TPBI) was prepared by polycondensation of 3,3'-diaminobenzidine and a triptycene-based diacid monomer. Subsequently, a facile approach was employed to boost the size-sieving ability by doping TPBI with H_3PO_4 to introduce strong intermolecular interactions. The TPBI and acid-doped TPBI composite membranes (TPBI-$(H_3PO_4)_x$) were systematically evaluated regarding microporosity and gas transport properties. We demonstrate that both pure-gas and mixed-gas separation properties of TPBIs are highly tailorable *via* adjusting the H_3PO_4 doping level, providing an attractive selectivity-driven engineering strategy allowing for superior gas separation performance.

2 Experimental

2.1 Materials

3,3'-Diaminobenzidine (DAB, ≥97%) was purchased from Sigma-Aldrich (Shanghai) and used as received. Phosphoric acid (PA, >98%) was purchased from Acros Organics (Shanghai). Phosphorus pentoxide (≥98%), methanesulfonic acid (99.5%), and anhydrous *N*,*N*-dimethylacetamide (99.8%) were purchased from Aladdin Chemical Co. (Beijing) and used without further treatment. The triptycene-containing diacid (TPD) monomer was synthesized following a previously reported procedure [27], and Eaton's reagent was produced by mixing phosphorus pentoxide with methanesulfonic acid (w/w: 1/10) at room temperature [36].

2.2 Synthesis of triptycene-containing polybenzimidazole (TPBI)

TPBI was synthesized by polycondensation between DAB and TPD in Eaton's reagent, which acted as the dehydrating agent and solvent. A mixture of DAB (0.4284 g, 4.0 mmol) and Eaton's reagent (17.0381 g) was added into a 100 mL three-necked flask under a nitrogen atmosphere. After complete dissolution of DAB, a stoichiometric amount of TPD (1.0531 g, 4.0 mmol) was added into the flask, and the mixture was stirred at 100 °C for 3 h and then 140 °C for 5 h. The reaction solution was precipitated in deionized water. The solid was then filtered, boiled in 5% $NaHCO_3$ solution, and deionized water, respectively, to remove residual reactants and salts. TPBI was collected after dried and vacuumed at 170 °C overnight. Yield: 95% (1.4073 g). ^{1}H NMR (600 MHz, DMSO-d_6): δ = 5.81 (s, 2H), 6.88 (s, 2H), 6.95 (m, 4H), 7.09 (m, 6H), 7.35 (s, 2H), 7.63 (m, 4H), 7.78 (s, 2H), 7.97 (s, 2H), 8.24(s, 4H), 12.95(s, 2H). ATR-

FTIR (membrane, ν, cm^{-1}): ~3300 (br, -NH), 1630 (C=N str) 1450 (imidazole ring). Molecular weight: $M_n = 7.6 \times 10^4$ g mol^{-1}, $M_w = 23.5 \times 10^4$ g mol^{-1}, PDI = 3.1 (Scheme 1).

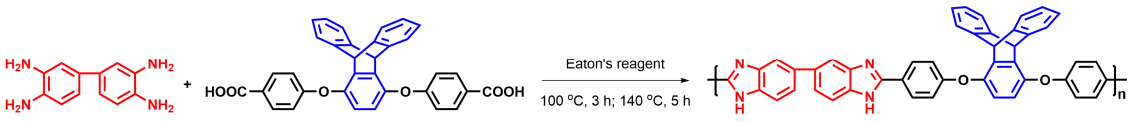

Scheme 1. Synthesis of TPBI *via* polycondensation between TPD and DAB

2.3 Membrane preparation

Dense TPBI membranes were obtained by the solution casting method. Specifically, 0.6 g of TPBI was entirely dissolved in 10 mL DMAc and filtered with a 0.45 μm syringe filter to eliminate any undissolved polymers or dust. The solution was cast onto a clean and pre-dried glass plate and heated using an infrared lamp at 60 °C for 14 h. The isotropic film was obtained and peeled off from the glass plate, and the film was further dried under vacuum at 170 °C for 4 h to evaporate the residual solvent completely. Free of solvent in all films was verified by thermogravimetric analysis (TGA).

The TPBI-PA composite membranes were fabricated by immersing the TPBI films (~25 μm) in PA/methanol solutions containing predetermined amounts of PA. The solution was stirred for 20 h and then dried in a vacuum oven at 110 °C for 4 h. The composite membranes are named TPBI-(H_3PO_4)-x, where x represents the PA weight content. The weights before and after PA treatment were recorded as m_0 and m_1, respectively, and the doping level was calculated using equation (1):

$$x = \frac{(m_1 - m_0)/M_{Acid}}{m_0/M_{PBI}} \quad (1)$$

2.4 Characterization

^{1}H NMR was acquired on a Bruker AVANCE III 600 MHz spectrometer, and the polymers were dissolved in deuterated dimethylsulfone (DMSO-d_6). Fourier transform infrared (FT-IR) spectra were obtained on a Thermo Nicolet-380 spectrometer in the wavenumber range of 400~4000 cm^{-1} and 32 scans in attenuated total reflection mode (ATR-FTIR). In situ FT-IR measurements were performed on a Bruker INVENIOR FT-IR spectrometer coupled with a diffuse reflectance cell (Harrick). Molecular weight and polymer dispersity index (PDI) were measured by gel permeation chromatography (GPC, Waters 1515) with DMF as the eluent. The surface and cross-sectional morphologies were imaged using a Hitachi SU8020 scanning electron microscope (SEM), and the element distribution within the film was analyzed using the energy dispersive spectrometer (EDS). Thermogravimetric analysis (TGA) was performed on a SHIMADZU apparatus (DTG-60H) in the temperature range of 100~800 ºC with a ramp rate of 10 °C min^{-1} under a N_2 purge rate of 30 mL min^{-1}. The mechanical properties of TPBI and TPBI-$(H_3PO_4)_x$ composite membranes were determined using a MTS-CMT6103 apparatus at room temperature according to the ASTM D-1708-13 standard. At least five specimens with a gauge length of 40 mm, an initial width of 10 mm, and a membrane thickness of 20~25 μm were measured, and the average values were recorded.

X-ray photoelectron spectroscopy (XPS, PHI5000 VersaprobeIII) was measured using Mono AlKa of 1486.6 eV under 15 kV voltage and 4.5 mA beam. The element content of phosphorus content was carried out by an inductively coupled plasma spectrometer (ICP-9000, SHIMADZU). Wide-angle X-ray diffraction (WAXD)

172 measurements were carried out using a Rigaku Smartlab(9) diffractometer with Cu Kα
173 radiation (wavelength λ = 1.54 Å) operated at 40 kV and 40 mA. The scan speed was
174 5° min^{-1}, the step size was 0.02° per step, and the average *d*-spacing was calculated by
175 Bragg's law. The densities of the membranes were measured using the buoyancy
176 method on an analytical balance (Mettler Toledo, ME204) coupled with a density kit.
177 The fractional free volume (FFV) was calculated as below:

178 $$FFV = \frac{V_0 - 1.3V_w}{V_0} \quad (2)$$

179 where V_0 is the occupied volume, and V_w represents the van der Waals volume [37].
180 The membrane thickness was obtained by a digital micrometer (Mitutoyo), and the
181 effective gas permeation area was acquired by a scanner (CanoScan LiDE 300) and
182 ImageJ software.

183 The positron annihilation lifetime spectroscopy (PALS) was performed at elevated
184 temperature on a fast-fast coincidence system with a time resolution of 200 ps in
185 FWHM [38]. The samples were prepared by cutting into ~1×1 cm membrane
186 specimens and stacked to 2 mm thickness. ^{22}Na was used as the positron source, and
187 the membrane was sandwiched by two 7.5 μm Kapton films. For accuracy, all PALS
188 data were measured twice under vacuum and analyzed using the CONTIN program.

189 Classical molecular dynamics (MD) simulation was performed with the
190 COMPASS force field. For each system, the simulation box was put into ten polymer
191 chains with five repeat units randomly at 298 K. Phosphoric acids were added according
192 to the ratio in the experiment. Firstly, the systems were optimized with the conjugate
193 gradient minimization algorithm to relax the chains. Then the simulation was performed

194 in an NPT (constant number of particles, pressure, and temperature) ensemble for 500
195 ps at 298 K and 1 atm with a V-rescale thermostat and Berendsen barostat. Finally, 100
196 ps production simulation was carried out at 298 K and 1 atm with a Nose thermostat
197 and barostat. The time step is 1 fs. Long-range electrostatic interaction and van der
198 Waals interaction were defined with a cutoff distance of 1.2 nm and managed by the
199 particle-particle particle-mesh (PPPM) method. The trajectory data was stored for every
200 1000 fs. LAMMPS was used to analyze the classical MD simulations. The visualized
201 Connolly surface and occupied volume were shown in Materials studio with a probe
202 radius of 2 Å.

203 The partial charge of benzimidazole and phosphoric acids was calculated using
204 Gaussian 16 code, and the 6-31+g(d,p) basis functions were applied [39]. The OPLSS-
205 AA force field and MKTOP [40] were used to parametrize all atoms.100 benzimidazole
206 molecules and 100 phosphoric acids were randomly distributed in a cube box with a
207 side length of 6.1 nm. The molecular dynamics (MD) simulation for the interaction
208 between the benzimidazole and phosphoric acid at different temperatures (50, 70, 100,
209 120, and 150 ^{o}C) was performed in the GROMACS 2019 software package [41-45],
210 and the simulation time is 10 ns. The initial energy for each system was minimized with
211 1 kJ mol^{-1} nm^{-1} force standard by 0.002 ps step length. Newtonian equation model was
212 performed by the leapfrog algorithm [46]. The Particle-Mesh-Ewald (PME) with a
213 fourth-order interpolation was used to evaluate the electrostatic interactions, and the
214 grid spacing is 1.0 Å [47], whereas the short-range van der Waals interaction was
215 defined with a maximum of 1.0 Å. LINCS algorithm was consulted to constrain the

hydrogen bond length and the number of hydrogen bonds between benzimidazole and phosphoric acid.

Pure gas permeabilities of He, H_2, CO_2, N_2, and CH_4 were measured at 35 °C and 100 PSIA feed pressure on a home-built gas permeation apparatus according to the constant-volume, variable pressure method [48]. All membranes were thoroughly degassed on both sides for more than 24 h before introducing ultra-high purity upstream. The downstream pressure increment was monitored, and the pure gas permeabilities were acquired as follows:

$$P = 10^{10} \frac{V_d l}{p_{up} TRA} \left[\left(\frac{dp}{dt} \right)_{ss} - \left(\frac{dp}{dt} \right)_{leak} \right] \quad (3)$$

where P (Barrer, 1 barrer = 10^{-10} cm^3 (STP) cm cm^{-2} s^{-1} $cmHg^{-1}$) represents the gas permeability, V_d (cm^3) is the downstream volume, l (cm) is membrane thickness, p_{up} (cmHg) is the upstream pressure, T(K) is the measurement temperature, R (0.278 cm^3 cmHg cm^{-3}(STP) K^{-1}) is the gas constant value, A (cm^2) is the effective film area, dp/dt represents the variation of downstream value related to time, and $(dp/dt)_{leak}$ is measured by the same method in a no-operation sealed permeation system. The ideal selectivity ($\alpha_{A/B}$) was defined as the permeability ratio of two gases (A and B):

$$\alpha_{A/B} = \frac{P_A}{P_B} \quad (4)$$

The diffusion coefficient (D) was determined from the time-lag method [48] as follows:

$$D = \frac{l^2}{6\theta} \quad (5)$$

where θ is the time-lag. The Solubility coefficient (S) was calculated based on the diffusion-solution model as follows:

$$S = \frac{P}{D} \quad (6)$$

The mixed-gas permeabilities were measured on the same equipment with a gas chromatograph (Agilent 8890 GC system) connected to the downstream chamber. A 50:50 H_2/CO_2 binary mixture was employed as the feed gas, and the sample cell temperature was regularly varied in the range of 35~150 °C. The high-pressure mixed-gas He/CH_4 separation performance of the TPBI membrane was evaluated using a 0.3:99.7 He/CH_4 binary mixture in the feed pressure range of 4~30 bar at 35 °C. The feed pressure was 100 PSIA, the permeate pressure was less than 10 Torr; the stage-cut was less than 0.01. Therefore, the concentration polarization in the feed can be avoided. The composition of the binary permeate gas mixture was determined using GC, and the mixed-gas permeability of gas A was calculated as the following equation:

$$P_A = 10^{10} \frac{y_A V_d l}{x_A p_{up} TRA} \frac{dp}{dt} \quad (7)$$

where *x*/*y* represent gas feed/permeate mole fraction. The mixed-gas selectivities were calculated as follows:

$$\alpha_{\mathrm{A/B}} = \frac{y_A / y_B}{x_A / x_B} \quad (8)$$

3 Results and discussion

3.1 Fabrication of H_3PO_4-doped TPBI membranes

TPBI was synthesized in high molecular weight *via* polycondensation between 3,3'-diaminobenzidine (DAB) and the triptycene-containing diacid (TPD) in Eaton's reagent with an optimized heating protocol [36, 49]. The TPBI polymer exhibited the anticipated chemical structure confirmed by ^{1}H NMR and FTIR (Figs. S1 and S2). The complete imidazole structure was verified by comparing the peak integrations between

the imidazole N-H proton (peak j, δ = 12.95) and the characteristic triptycene bridgehead proton (peak d, δ = 5.81). The characteristic benzimidazole structure was also confirmed by the C=N stretching at 1630 cm^{-1} and the imidazole ring vibration at 1450 cm^{-1} in FTIR spectra. TPBI displayed a high weight-average molecular weight of 234, 900 Da and a polydispersity index of 3.1, ensuring the fabrication of robust membranes. The geometrically optimized TPBI chain segments reveal the contorted conformation (Fig. 1a).

A previous study demonstrated that excess doping of H_3PO_4 would severely deteriorate the mechanical strength of the composite membranes by swelling PBI segments, especially at high temperatures [50]. As such, the doping level (x = 0.33~1.46) was controlled and systematically varied by immersing the TPBI films in H_3PO_4/methanol solutions with different concentrations (Table S1). The even distribution of phosphorus was imaged with overlaid SEM/EDS mapping on the film surface and cross-section (Fig. 1c and 1d), revealing that the TPBI-$(H_3PO_4)_x$ composite membranes were homogeneously doped with H_3PO_4. The TPBI-$(H_3PO_4)_x$ composite membranes, especially with high doping levels (x = 0.98 and 1.46), showed much improved mechanical properties as compared to pristine TPBI film, likely due to enhanced inter-chain interaction related to proton transfer and hydrogen bonding between the acid and imidazole rings (Figs. 1e and S3). This is evidenced by the appearance of $H_2PO_4^-$ bands in the FTIR spectra with the characteristic peaks of PO_2 (1050 cm^{-1}) and $P(OH)_2$ (870 and 945 cm^{-1}) (Fig. 2a) [51].

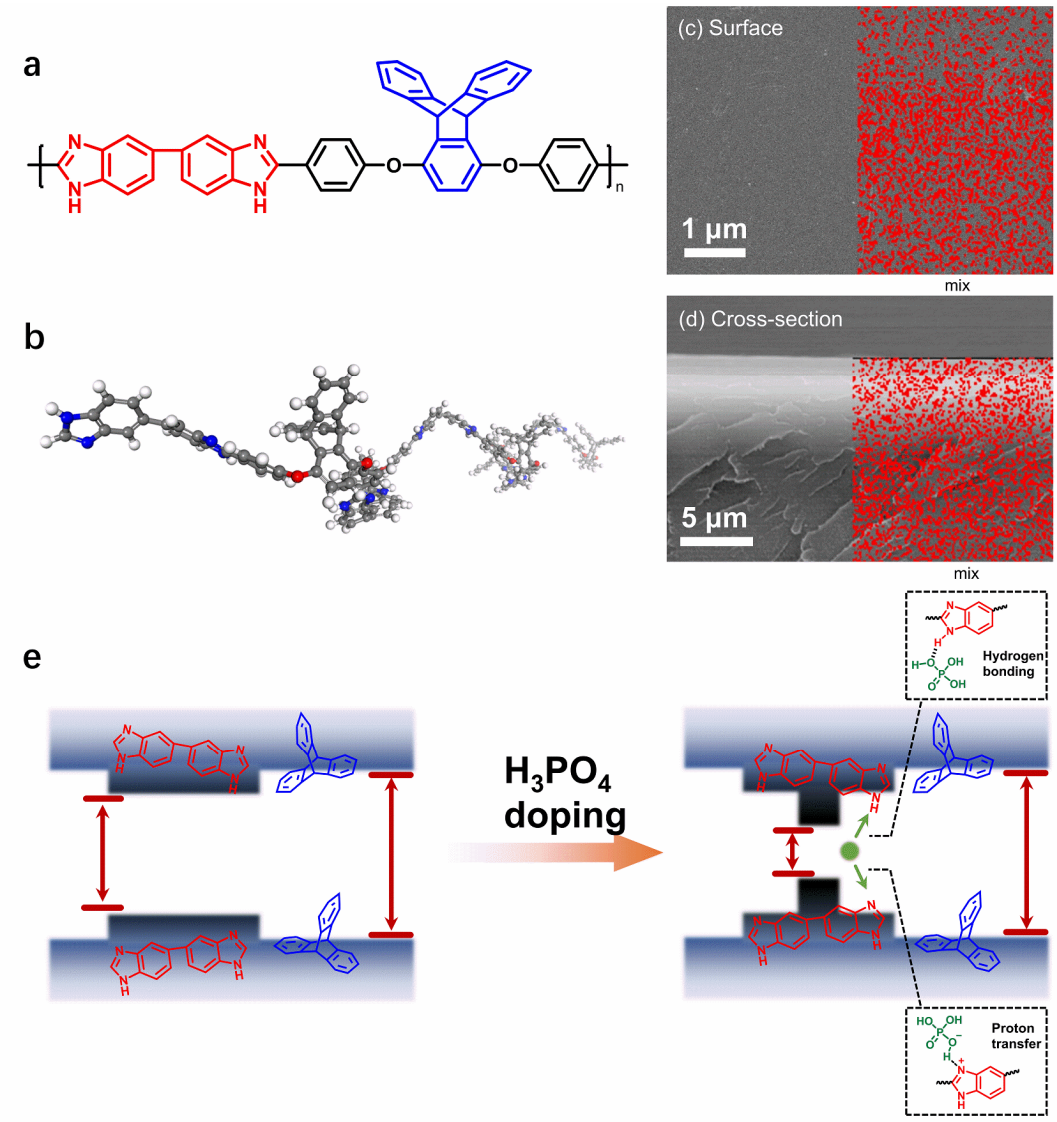

Fig. 1 (a) Chemical structure and (b) geometrically optimized chain segment of TPBI. The SEM images of (c) surface and (d) cross-section of TPBI-$(H_3PO_4)_{0.98}$ membrane with EDS mapping show homogeneous phosphorus distribution (red dots). (e) Schematic illustration of the interaction between TPBI and H_3PO_4.

The thermal stability of TPBI-$(H_3PO_4)_x$ membranes was evaluated by thermal gravimetric analysis (TGA). As shown in Fig. 2b and Table S1, the TPBI-$(H_3PO_4)_x$ composite membranes displayed the starting degradation temperatures of more than 200 °C and a two-stage weight loss profile. The first-stage weight losses increase with the doping level and correspond well with the phosphoric acid to pyrophosphoric acid conversion, which releases H_2O at elevated temperatures (200~500 °C) [52]. The

drastic weight loss after 500 °C is ascribed to the degradation of the PBI backbone. WAXD measurements were performed to illustrate the effect of H_3PO_4 doping on the PBI chain packing for TPBI-$(H_3PO_4)_x$ composite membranes (Fig. 2c). The precursor TPBI membrane exhibits a broad diffraction peak at 19.3°, corresponding to an average inter-segmental distance (i.e., *d*-spacing) of ~4.6 Å. The *d*-spacing values decrease with the increase of doping level, implying the hydrogen bonding and proton transfer promoted tight chain packing resulting in smaller average inter-segmental distances. Compared with previously reported non-triptycene containing PBI and PBI-$(H_3PO_4)_x$ composite membranes (e.g., *m*-PBI and *m*-PBI-$(H_3PO_4)_x$ [24]), the *d*-spacing values of the TPBI and TPBI-$(H_3PO_4)_x$ membranes are higher at the same doping level, confirming that rigid hierarchical triptycene moieties effectively disrupted chain packing. As discussed later, decreasing *d*-spacing values with the increasing doping level would inevitably lead to increased size sieving ability.

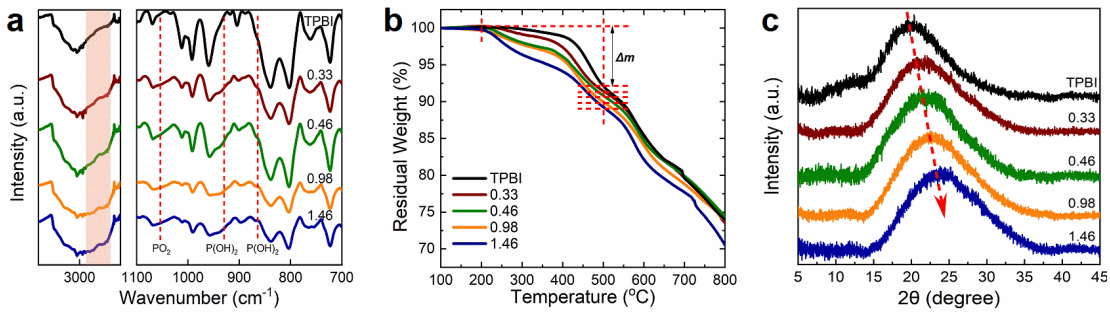

Fig. 2 (a) FTIR spectra, (b) TGA profiles, and (c) WAXD patterns of the TPBI-$(H_3PO_4)_x$ membranes. The numbers in the figure represent the doping level.

The microporosity of TPBI-$(H_3PO_4)_x$ membranes was characterized by positron annihilation lifetime spectroscopy (PALS), which measures the lifetime of spin-triplet positroniums (*o*-Ps) trapped in polymer free volume elements and correlates it with the size of the micropores [38]. The temperature dependence of the *o*-Ps lifetime of

membranes was analyzed using the CONTIN program. As shown in Fig. 3d-f, TPBI, TPBI-$(H_3PO_4)_{0.46}$ and TPBI-$(H_3PO_4)_{0.98}$ membranes displayed a unimodal pore size distribution centered at 6.4, 6.1, and 5.9 Å, respectively, at 35 °C, and shifted to 6.9, 6.3 and 6.0 Å, respectively, at 150 °C. As the doping level increased, membrane pore size became smaller due to tighter chain packing *via* hydrogen bond. In addition, the microporous structure of the TPBI membrane series was simulated to illustrate their microporosity. As shown in Fig. 3a, TPBI showed a large accessible surface area and fraction free volume (FFV) induced by the rigid triptycene moieties. The overall FFV became smaller and more uniform after H_3PO_4 doping, which confirmed the hydrogen bonding induced PBI chain tightening by H_3PO_4 (Fig. 3b and 3c). All membranes exhibited larger average pore sizes at elevated temperatures (Fig. 3d-f) primarily due to thermal expansion [24], corresponding well with the results of in situ WAXD analysis (Fig. S4) and gas permeability data (Table S2). The less significant increase in the average pore size with temperature for the TPBI-$(H_3PO_4)_{0.46}$ and TPBI-$(H_3PO_4)_{0.98}$ membranes can be ascribed to the hydrogen bonding-induced enhancement of inter-chain interaction and the restriction of segmental motion.

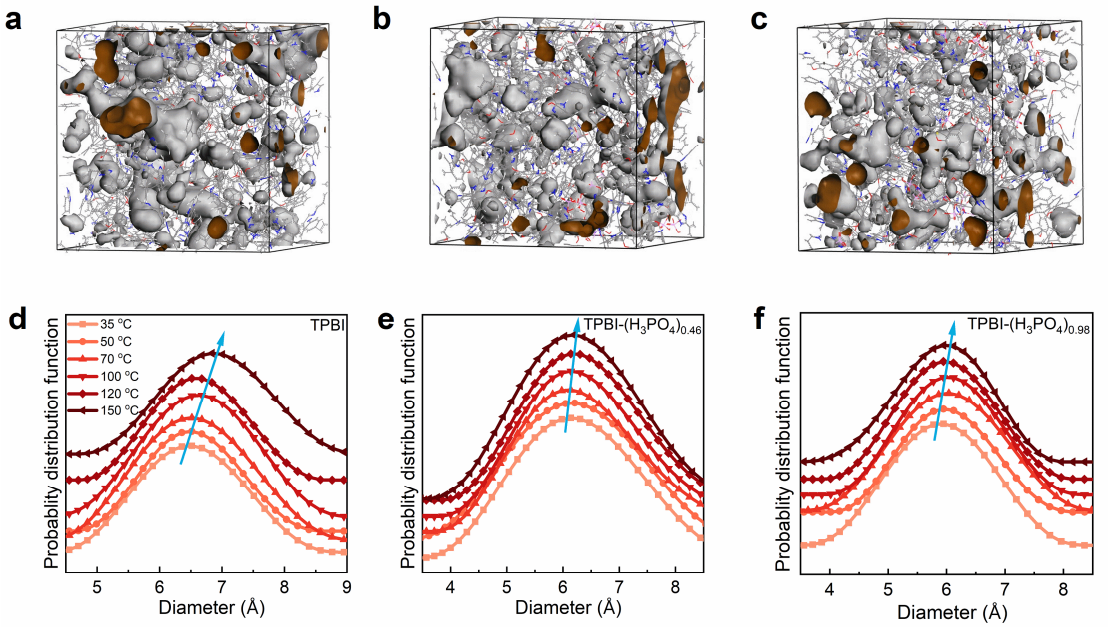

328

329 **Fig. 3** Computational modeling of microporous surfaces and corresponding pore-size
330 distributions at elevated temperatures obtained from PALS for (a), (d) TBPI, (b), (e)
331 TPBI-$(H_3PO_4)_{0.46}$, and (c), (f) TPBI-$(H_3PO_4)_{0.98}$ membranes. (Tubular regions in a-c
332 represent the accessible surface area or free volume in membranes.)

333 **3.2 Gas transport properties**

334 Pure-gas transport properties of TPBI and TPBI-$(H_3PO_4)_x$ composite membranes
335 were tested at 35 °C and 100 PSIA, and the results are shown in Table S3 and Fig. 4.
336 Pure-gas permeabilities of membranes follow the order of gas kinetic diameter (i.e.,
337 He>H_2>CO_2>O_2>N_2>CH_4), suggesting that diffusivity plays a dominant role in
338 permeation (Fig. 4a). Remarkably, the TPBI membrane exhibits much higher gas
339 permeabilities than non-triptycene-containing PBI membranes due to the incorporation
340 of configurational free volume and the disruption of chain packing by the rigid and 3D
341 structure of triptycene units. For instance, the H_2 permeability of the TPBI membrane
342 is 86 and 16 times those of the benchmark *m*-PBI [53] and TADPS-IPA [54],
343 respectively. As depicted in Fig. 4a and 4b, increasing the doping level decreases pure-

gas permeabilities and significantly increases H_2 and He-related gas selectivities. Specifically, pristine TPBI shows the H_2/CH_4 and He/CH_4 selectivities of 385 and 301, respectively, and the selectivity increases drastically with the doping level. The membrane with the highest doping level, i.e., TPBI-$(H_3PO_4)_{1.46}$, displays the highest selectivity of 5128 significantly for H_2/CH_4 and 7052 for He/CH_4 with the He and H_2 permeabilities of 5.0 and 3.6 Barrer, respectively, and the selectivities are among the highest values of any reported polymer membranes. The H_2/CO_2 selectivity increased 30 times from 2.2 in pristine TPBI film to 62.3 at the highest doping level of 1.46. The enhancement of gas selectivity with increasing doping level could be ascribed to the boosted size-sieving ability where much tighter chain packing enabled by strong H-bonding significantly restricted the transport of large gases like CH_4 and CO_2 with much less impact on H_2 transport. Although the average pore sizes obtained from PALS measurements were larger than the kinetic diameters of CO_2 and H_2, the high H_2/CO_2 selectivities of the TPBI-$(H_3PO_4)_x$ membranes suggested that the connections of microvoids, or "bottlenecks," plays a crucial role for size sieving [55]. This is evidenced by the remarkable increase of diffusivity selectivity with doping level (Fig. S5). Additionally, the diffusivity coefficient correlated well with the kinetic diameters of the six testing gases (Fig. S6), demonstrating the dominant role of molecular sieving towards gas separation in TPBI-$(H_3PO_4)_x$ membranes.

Pure-gas permeabilities were further correlated with FFV using the following equation:

$$P = A\exp(-B/FFV) \qquad (9)$$

where A and B represent the pre-exponential factor and the penetrant size-related constant, respectively [56]. As shown in Table S4 and Fig. 4c, increasing the H_3PO_4 doping level increases the membrane density and thus decreases the FFV, and the pure-gas permeabilities can be sufficiently depicted with Equation 9. Specifically, it is observed that H_2 and He display much lower B values than the other gases (Table S5), suggesting that H_2 and He permeabilities are less sensitive to FFV reduction due to their smaller sizes. The larger B values of CO_2, N_2, and CH_4 resulted in a more rapid decrease in gas permeabilities and an exponential increase in H_2/CO_2, H_2/N_2, H_2/CH_4, He/N_2, and He/CH_4 selectivities (Table S3). Specifically, the TPBI-$(H_3PO_4)_{1.46}$ membrane with the lowest FFV of 0.150 exhibited He and H_2 permeabilities of 5.0 and 3.6 Barrer, respectively, and the highest H_2/CO_2, H_2/N_2, H_2/CH_4, He/N_2, and He/CH_4 selectivities of 62.3, 2562, 5128, 3524, and 7052, respectively, among any reported polymeric membranes. In this regard, the TPBI-$(H_3PO_4)_x$ composite membranes hold great potential for H_2 and He recovery.

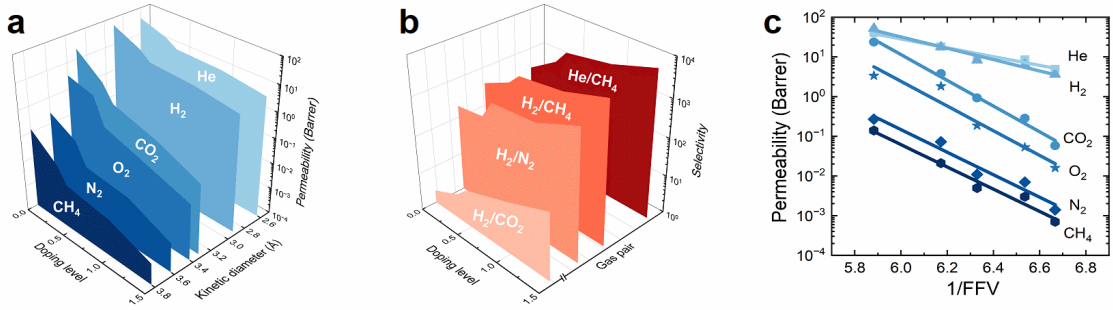

Fig. 4 Pure-gas a) permeability as a function of doping level and gas kinetic diameter, b) selectivity for various gas pairs, and c) permeability as a function of 1/FFV.

PBI-based membranes have shown great potential for H_2 recovery from coal-derived shifted syngas, typically operated at high temperatures (150 °C or above) [10]. The temperature dependence of pure-gas transport properties of TPBI and TPBI-

386 $(H_3PO_4)_x$ membranes were measured in the temperature range of 50~150 °C with the
387 feed pressure of 100 PSIA (Fig. 5 and Table S2). TPBI-$(H_3PO_4)_{0.98}$ was selected as a
388 model membrane to highlight the effect of acid-doping-induced inter-chain interactions
389 considering its stoichiometric doping of H_3PO_4. Pure-gas H_2 and CO_2 permeabilities of
390 both the TPBI and TPBI-$(H_3PO_4)_{0.98}$ membranes increased with the increasing
391 temperature due to the significant enhancement of diffusivity coefficients, which is
392 consistent with the increased *d*-spacing values and decreased interchain interaction
393 induced by hydrogen bonding (Fig. S4a-e,). A monotonic increase of the H_2/CO_2
394 selectivity with temperature was observed for the TPBI membrane, which can be
395 ascribed to a more significant contribution of solubility selectivity relative to the
396 diffusivity selectivity at elevated temperatures (Fig. S7) [57]. The considerable decrease
397 of diffusivity selectivity at 70 °C resulted in a reduced H_2/CO_2 selectivity for the TPBI-
398 $(H_3PO_4)_{0.98}$ membrane. The H_2/CO_2 selectivity remained almost constant above 70 °C
399 (Fig. 5b). The results are consistent with the simulated number of hydrogen bonding
400 (Fig. S4f), which was lower by 10% below 70 °C, and kept invariant over 70 °C [58,
401 59].

402 The pure- and mixed-gas permeabilities of H_2 and CO_2 exhibited significant
403 Arrhenius regression with temperature for both membranes (Fig. 5c and 5d). In
404 particular, CO_2 displayed a smaller permeability increase than H_2 with temperature,
405 most likely due to the diminished sorption of CO_2 at elevated temperatures. The H_2 and
406 CO_2 activation energies were obtained, and the results are shown in Table S6. The TPBI
407 membrane showed the H_2 and CO_2 activation energy of 15.7 and 7.5 kJ mol^{-1},

respectively, and the much smaller CO_2 activation energy revealed strong TPBI-CO_2 interactions [60]. For TPBI-$(H_3PO_4)_{0.98}$ membrane, the E_p of CO_2 is slightly higher than H_2, resulting in minor H_2/CO_2 selectivity variations with temperatures above 70 °C.

The TPBI-$(H_3PO_4)_x$ membranes also demonstrated outstanding gas separation performance for helium extraction from natural gas and ammonia separations (NH_3/CO_2 and NH_3/N_2, Table S3). For instance, the TPBI-$(H_3PO_4)_x$ membranes displayed He permeability of 5~41 Barrer with He/CH_4 selectivity of 301~7052; notably, the TPBI-$(H_3PO_4)_{1.46}$ membrane showed the highest pure-gas He/CH_4 selectivity so far reported for all existing polymer membranes. Monotonic increases of He/N_2 and He/CH_4 selectivities with doping levels were observed, confirming the significantly boosted size sieving *via* H_3PO_4-induced hydrogen bonding and proton transfer. Interestingly, the TPBI membrane also showed an NH_3 permeability of 275 Barrer, NH_3/CO_2 and NH_3/N_2 selectivity of 11.5 and 24, respectively, suggesting great potential in NH_3 separation from ammonia production (Table S3).

Mixed-gas separation performance of the TPBI-$(H_3PO_4)_x$ membranes was evaluated using a binary gas mixture of 50:50 (v/v) H_2/CO_2 at 50~150 °C with a total feed pressure of 100 PSIA. As depicted in Fig. 5 and Table S2, both TPBI and TPBI-$(H_3PO_4)_{0.98}$ membranes displayed mixed-gas transport properties (open symbols) very close to the pure-gas performance (solid symbols) over the full range of testing temperatures. Specifically, the TPBI-$(H_3PO_4)_{0.98}$ membrane exhibited a mixed-gas H_2 permeability of 45.5 Barrer and a high H_2/CO_2 selectivity of 15.4 at 150 °C, confirming the great potential of the TPBI-$(H_3PO_4)_x$ membranes for H_2/CO_2 separation at high

temperatures. Minor variations between mixed-gas and pure-gas H_2/CO_2 selectivities with temperature were observed for the TPBI and TPBI-$(H_3PO_4)_{0.98}$ membranes due to the competition between solubility selectivity and diffusivity selectivity contributions, whereby increasing temperature increases H_2/CO_2 solubility selectivity and decreases size-sieving ability. The TPBI membrane also demonstrated excellent high-pressure mixed-gas He/CH_4 separation performance (Fig. S8).

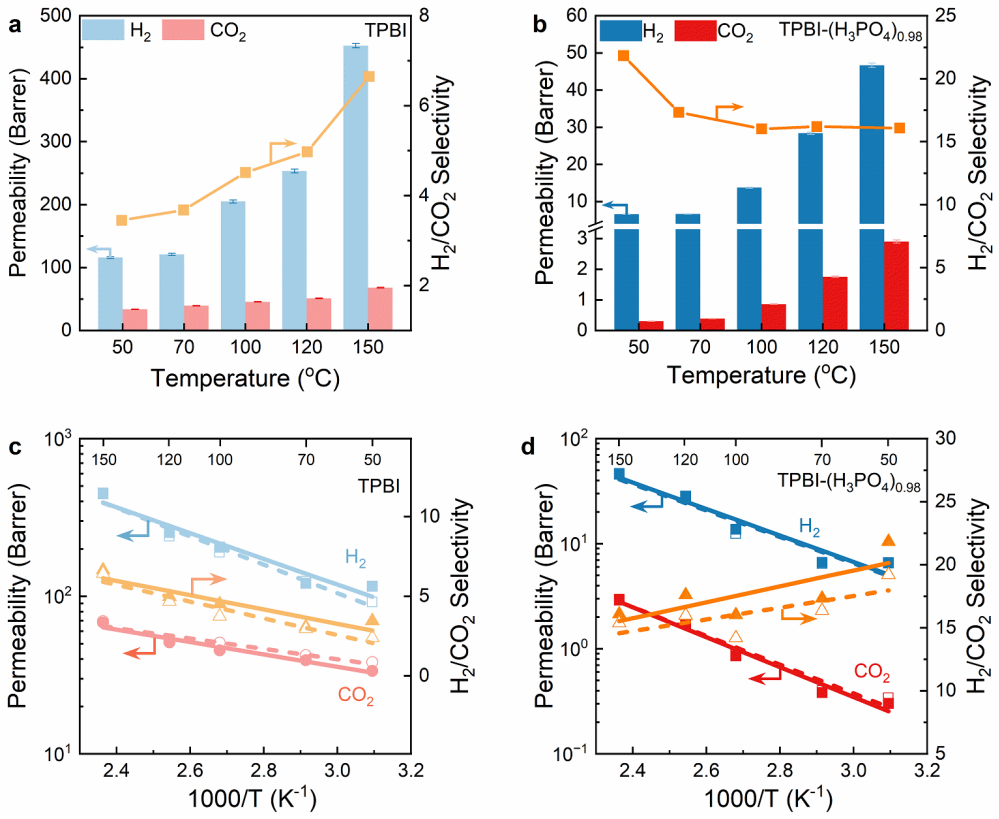

Fig. 5 Temperature dependence of pure- and mixed-gas permeabilities and H_2/CO_2 selectivities for a) c) TPBI and b) d) TPBI-$(H_3PO_4)_{0.98}$ membranes. Gas separation performance is plotted with Arrhenius regression, where solid lines and filled symbols are for pure-gas, and dashed lines and open symbols are for mixed-gas.

Pure- and mixed-gas separation performance of the TPBI-$(H_3PO_4)_x$ membranes compared to state-of-the-art polymeric membranes are summarized in Robeson's permeability/selectivity trade-off plots for H_2-related separations. The TPBI-$(H_3PO_4)_x$ membranes outperform the 2008 upper bounds [61] and approach the 2015 upper

445 bounds [31] for H_2/N_2 and H_2/CH_4 separations, revealing their superior separation
446 performance for H_2 recovery (Fig. 6). Interestingly, the H_2/CO_2 selectivity increased
447 dramatically with increasing doping level, consistent with the notion that H_3PO_4 doping
448 significantly increases size sieving. The mixed-gas permeation properties of the TPBI
449 and TPBI-$(H_3PO_4)_{0.98}$ membranes for H_2/CO_2 separation operating at 150 °C are far
450 exceeding the upper bound predicted for 150 °C [57] when tested under industrially
451 relevant conditions. Compared with commercial polymer membranes (e.g., Matrimid®
452 and polysulfone [17]), TPBI-$(H_3PO_4)_x$ membranes show superior H_2 permeability and
453 H_2/CO_2, H_2/N_2 and H_2/CH_4 selectivities. Compared with other reported PBI structures
454 (Table S7), TPBI-$(H_3PO_4)_x$ membranes exhibit ~10 times H_2/N_2 and H_2/CH_4
455 selectivities higher than those membranes and ~2-15 times H_2 permeability higher in
456 H_2/CO_2 separation. At the same H_3PO_4 doping level, TPBI-$(H_3PO_4)_{0.98}$ is 30 times more
457 permeable than *m*-PBI-$(H_3PO_4)_{1.0}$ [24], signifying the role of hierarchical triptycene
458 units in promoting H_2 transport and size-sieving properties. Compared to other state-
459 of-the-art materials (e.g., MOFs [62, 63], polymer mixed matrix membranes [64-66]
460 and interfacial polymerization membranes [60, 67]) that were also adopted for H_2/CO_2
461 separation, the TPBI-$(H_3PO_4)_x$ membranes reported in this work are much
462 advantageous due to the easiness and feasibility of membrane fabrication and scale-up
463 that is invaluable for practical implementation of novel membrane materials for
464 hydrogen purifications.

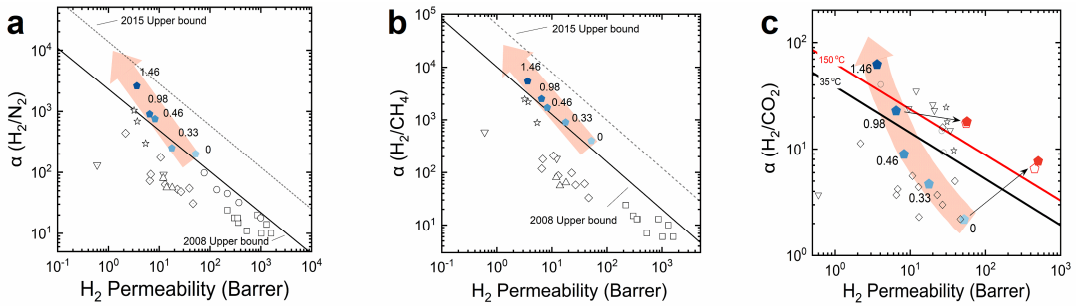

Fig. 6 Gas separation performance of TPBI-$(H_3PO_4)_x$ membranes with different doping levels for a) H_2/N_2, b) H_2/CH_4, and c) H_2/CO_2 separations. Solid lines are Robeson's 2008 upper bound [61], and dashed lines are 2015 upper bounds at 35 °C [31]. The red line is predicted H_2/CO_2 upper bound at 150 °C [57]. Blue data points represent pure-gas permeation data at 35 °C and red data points at 150 °C. Pure- and mixed-gas data points are signed as filled and open symbols, respectively. Also included for comparisons are *m*-PBIs and derived membranes (▽), 6F-PBIs (○), sulfone-PBIs (☆), alkyl-PBIs (◇), PIMs (□) and relevant commercial polymers (Matrimid, Polysulfone, and CA, △).

3 Conclusions

Polybenzimidazole membranes with unprecedentedly high gas selectivities and permeabilities were successfully fabricated in this study by incorporating hierarchical triptycene moieties and H_3PO_4 doping. The triptycene units disrupt chain packing and generate additional configurational free volumes, leading to substantially boosted He and H_2 permeabilities compared to previously reported PBI membranes. The acid doping resulted in physically crosslinked PBI membranes *via* hydrogen bonding and proton transfer with dramatically enhanced gas selectivities. Therefore, the TPBI-$(H_3PO_4)_{1.46}$ membrane displays the highest gas selectivities for He enrichment (i.e., $\alpha(He/CH_4)$ = 7052) and H_2 purification (i.e., $\alpha(H_2/CH_4)$ = 5128) among existing polymeric gas separation membranes. Notably, the microporosity and gas permeation properties are highly tailorable by regulating the H_3PO_4 doping level. The TPBI-$(H_3PO_4)_{0.98}$ membrane shows a mixed-gas H_2 permeability of 46.7 Barrer and an H_2/CO_2 selectivity of 16 at 150 °C, which exceeds state-of-the-art polymeric materials for H_2/CO_2 separation. The facile and diverse tunability and excellent gas separation performance demonstrate novel macromolecular engineering to manipulate microporosity and gas transport for highly energy-efficient and practical helium enrichment and hydrogen purification.

Acknowledgments

S. Luo and S. Zhang acknowledge the financial support from the National Natural Science Foundation of China (22008243, 12275270), Beijing Nova Program of Science and Technology (Z191100001119107), and the International Partner Program of CAS (122111KYSB20200035). M.L. and R.G. acknowledge the financial support by the Division of Chemical Sciences, Biosciences, and Geosciences, Office of Basic Energy Sciences of the U.S. Department of Energy (DOE), under award no. DE-SC0019024.

References

[1] M. Sevilla, R. Mokaya, Energy storage applications of activated carbons: Supercapacitors and hydrogen storage, Energy Environ. Sci., 7 (2014) 1250-1280.

[2] L. Schlapbach, A. Züttel, Hydrogen-storage materials for mobile applications, Nature, 414 (2001) 353-358.

[3] L. Cai, Z. Cao, X. Zhu, W. Yang, Improved hydrogen separation performance of asymmetric oxygen transport membranes by grooving in the porous support layer, Green Chem. Eng., 2 (2021) 96-103.

[4] X. Chen, G.P. Liu, W.Q. Jin, Natural gas purification by asymmetric membranes: An overview, Green Energy Environ., 6 (2021) 176-192.

[5] S. Mohammed, H.H. M, R. Ou, S. Liu, H. Ma, X. Chen, T. Sridhar, H. Wang, Effect of oxygen plasma treatment on the nanofiltration performance of reduced graphene oxide/cellulose nanofiber composite membranes, Green Chem. Eng., 2 (2021) 122-131.

[6] H.K. Knuutila, R. Rennemo, A.F. Ciftja, New solvent blends for post-combustion CO_2 capture, Green Energy Environ., 4 (2019) 439-452.

[7] M.G. Jackson, J.G. Konter, T.W. Becker, Primordial helium entrained by the hottest mantle plumes, Nature, 542 (2017) 340-343.

[8] H.B. Park, J. Kamcev, L.M. Robeson, M. Elimelech, B.D. Freeman, Maximizing the right stuff: The trade-off between membrane permeability and selectivity, Science, 356 (2017) eaab0530.

[9] C.A. Scholes, U. Ghosh, Helium separation through polymeric membranes: Selectivity targets, J. Membr. Sci., 520 (2016) 221-230.

[10] T.C. Merkel, M. Zhou, R.W. Baker, Carbon dioxide capture with membranes at an IGCC power plant, J. Membr. Sci., 389 (2012) 441-450.

[11] H.W. Kim, H.W. Yoon, S.-M. Yoon, B.M. Yoo, B.K. Ahn, Y.H. Cho, H.J. Shin, H. Yang, U. Paik, S. Kwon, J.-Y. Choi, H.B. Park, Selective gas transport through few-layered graphene and graphene oxide membranes, Science, 342 (2013) 91-95.

[12] W. An, P. Swenson, L. Wu, T. Waller, A. Ku, S.M. Kuznicki, Selective separation of hydrogen from C1/C2 hydrocarbons and CO_2 through dense natural zeolite

533 membranes, J. Membr. Sci., 369 (2011) 414-419.
534 [13] X. Liu, D. He, Atomic layer deposited aluminium oxide membranes for selective
535 hydrogen separation through molecular sieving, J. Membr. Sci., 662 (2022) 121011.
536 [14] A. Akbari, J. Karimi-Sabet, S.M. Ghoreishi, Intensification of helium separation
537 from CH_4 and N_2 by size-reduced cu-btc particles in Matrimid matrix, Sep. Purif.
538 Technol., 251 (2020) 117317.
539 [15] J.Y. Kim, H. Oh, H.R. Moon, Hydrogen isotope separation in confined nanospaces:
540 Carbons, zeolites, metal-organic frameworks, and covalent organic frameworks, Adv.
541 Mater., 31 (2019) 1805293.
542 [16] C. Zhu, Y. Peng, W. Yang, Modification strategies for metal-organic frameworks
543 targeting at membrane-based gas separations, Green Chem. Eng., 2 (2021) 17-26.
544 [17] D.E. Sanders, Z.P. Smith, R. Guo, L.M. Robeson, J.E. McGrath, D.R. Paul, B.D.
545 Freeman, Energy-efficient polymeric gas separation membranes for a sustainable future:
546 A review, Polymer, 54 (2013) 4729-4761.
547 [18] X. Wang, M. Shan, X. Liu, M. Wang, C.M. Doherty, D. Osadchii, F. Kapteijn,
548 High-performance polybenzimidazole membranes for helium extraction from natural
549 gas, ACS Appl. Mater. Inter., 11 (2019) 20098-20103.
550 [19] M. Shan, X. Liu, X. Wang, Z. Liu, H. Iziyi, S. Ganapathy, J. Gascon, F. Kapteijn,
551 Novel high performance poly(p-phenylene benzobisimidazole) (PBDI) membranes
552 fabricated by interfacial polymerization for H_2 separation, J. Mater. Chem. A, 7 (2019)
553 8929-8937.
554 [20] J.C. Chen, Y.R. Hsiao, Y.C. Liu, P.Y. Chen, K.H. Chen, Polybenzimidazoles
555 containing heterocyclic benzo[c]cinnoline structure prepared by sol-gel process and
556 acid doping level adjustment for high temperature pemfc application, Polymer, 182
557 (2019) 121814.
558 [21] S. Kumar B., B. Sana, G. Unnikrishnan, T. Jana, S. Kumar K. S.,
559 Polybenzimidazole co-polymers: Their synthesis, morphology and high temperature
560 fuel cell membrane properties, Polym. Chem., 11 (2020) 1043-1054.
561 [22] K. Geng, Y. Li, Y. Xing, L. Wang, N. Li, A novel polybenzimidazole membrane
562 containing bulky naphthalene group for vanadium flow battery, J. Membr. Sci., 586

563 (2019) 231-239.
564 [23] L. Zhu, M.T. Swihart, H. Lin, Tightening polybenzimidazole (PBI) nanostructure
565 *via* chemical crosslinking for membrane H_2/CO_2 separation, J. Mater. Chem. A, 5 (2017)
566 19914-19923.
567 [24] L. Zhu, M.T. Swihart, H. Lin, Unprecedented size-sieving ability in
568 polybenzimidazole doped with polyprotic acids for membrane H_2/CO_2 separation,
569 Energy Environ. Sci., 11 (2018) 94-100.
570 [25] S.S. Hosseini, M.M. Teoh, T.S. Chung, Hydrogen separation and purification in
571 membranes of miscible polymer blends with interpenetration networks, Polymer, 49
572 (2008) 1594-1603.
573 [26] S. Luo, Q. Zhang, L. Zhu, H. Lin, B.A. Kazanowska, C.M. Doherty, A.J. Hill, P.
574 Gao, R. Guo, Highly selective and permeable microporous polymer membranes for
575 hydrogen purification and CO_2 removal from natural gas, Chem. Mater., 30 (2018)
576 5322-5332.
577 [27] S. Luo, J. Liu, H. Lin, B.A. Kazanowska, M.D. Hunckler, R.K. Roeder, R. Guo,
578 Preparation and gas transport properties of triptycene-containing polybenzoxazole
579 (PBO)-based polymers derived from thermal rearrangement (TR) and thermal
580 cyclodehydration (TC) processes, J. Mater. Chem. A, 4 (2016) 17050-17062.
581 [28] S. Luo, Q. Liu, B. Zhang, J.R. Wiegand, B.D. Freeman, R. Guo, Pentiptycene-
582 based polyimides with hierarchically controlled molecular cavity architecture for
583 efficient membrane gas separation, J. Membr. Sci., 480 (2015) 20-30.
584 [29] B.S. Ghanem, R. Swaidan, E. Litwiller, I. Pinnau, Ultra-microporous triptycene-
585 based polyimide membranes for high-performance gas separation, Adv. Mater., 26
586 (2014) 3688-3692.
587 [30] M. Carta, M. Croad, R. Malpass Evans, J.C. Jansen, P. Bernardo, G. Clarizia, K.
588 Friess, M. Lanc, N.B. McKeown, Triptycene induced enhancement of membrane gas
589 selectivity for microporous troger's base polymers, Adv. Mater., 26 (2014) 3526-3531.
590 [31] R. Swaidan, B. Ghanem, I. Pinnau, Fine-tuned intrinsically ultramicroporous
591 polymers redefine the permeability/selectivity upper bounds of membrane-based air
592 and hydrogen separations, ACS Macro Lett., 4 (2015) 947-951.

[32] T.J. Corrado, Z. Huang, D. Huang, N. Wamble, T. Luo, R. Guo, Pentiptycene-based ladder polymers with configurational free volume for enhanced gas separation performance and physical aging resistance, Proc. Natl. Acad. Sci. U.S.A., 118 (2021) e2022204118.

[33] M.D. Guiver, Y.M. Lee, Polymer rigidity improves microporous membranes, Science, 339 (2013) 284-285.

[34] W.J. Koros, C. Zhang, Materials for next-generation molecularly selective synthetic membranes, Nat. Mater., 16 (2017) 289-297.

[35] B.S. Ghanem, R. Swaidan, X. Ma, E. Litwiller, I. Pinnau, Energy-efficient hydrogen separation by AB-type ladder-polymer molecular sieves, Adv. Mater., 26 (2014) 6696-6700.

[36] P.E. Eaton, G.R. Carlson, J.T. Lee, Phosphorus pentoxide-methanesulfonic acid. Convenient alternative to polyphosphoric acid, J. Org. Chem., 38 (1973) 4071-4073.

[37] A. Bondi, Van der waals volumes and radii, J. Phys. Chem., 68 (1964) 441-451.

[38] H. Zhang, S. Sellaiyan, T. Kakizaki, A. Uedono, Y. Taniguchi, K. Hayashi, Effect of free-volume holes on dynamic mechanical properties of epoxy resins for carbon-fiber-reinforced polymers, Macromolecules, 50 (2017) 3933-3942.

[39] G.A. Petersson, M.A. Allaham, A complete basis set model chemistry .2. Open-shell systems and the total energies of the 1st-row atoms, J. Chem. Phys., 94 (1991) 6081-6090.

[40] W.L. Jorgensen, D.S. Maxwell, J. Tirado Rives, Development and testing of the opls all-atom force field on conformational energetics and properties of organic liquids, J. Am. Chem. Soc., 118 (1996) 11225-11236.

[41] D. Van Der Spoel, E. Lindahl, B. Hess, G. Groenhof, A.E. Mark, H.J.C. Berendsen, Gromacs: Fast, flexible, and free, J. Comput. Chem., 26 (2005) 1701-1718.

[42] B. Hess, C. Kutzner, D. Van Der Spoel, E. Lindahl, Gromacs 4: Algorithms for highly efficient, load-balanced, and scalable molecular simulation, J. Chem. Theory Comput., 4 (2008) 435-447.

[43] S. Pronk, S. Páll, R. Schulz, P. Larsson, P. Bjelkmar, R. Apostolov, M.R. Shirts, J.C. Smith, P.M. Kasson, D. Van Der Spoel, B. Hess, E. Lindahl, Gromacs 4.5: A high-

623 throughput and highly parallel open source molecular simulation toolkit,
624 Bioinformatics, 29 (2013) 845-854.
625 [44] M.J. Abraham, T. Murtola, R. Schulz, S. Páll, J.C. Smith, B. Hess, E. Lindahl,
626 Gromacs: High performance molecular simulations through multi-level parallelism
627 from laptops to supercomputers, SoftwareX, 1-2 (2015) 19-25.
628 [45] S. Páll, M.J. Abraham, C. Kutzner, B. Hess, E. Lindahl, Tackling exascale software
629 challenges in molecular dynamics simulations with gromacs, in: Lecture notes in
630 computer science, Springer International Publishing, 2015, pp. 3-27.
631 [46] W.F. Van Gunsteren, H.J.C. Berendsen, A leapfrog algorithm for stochastic
632 dynamics, Mol. Simulat., 1 (1988) 173-185.
633 [47] T. Darden, D. York, L. Pedersen, Particle mesh ewald: An $N \cdot \log(N)$ method for
634 ewald sums in large systems, J. Chem. Phys., 98 (1993) 10089-10092.
635 [48] H. Lin, B. Freeman, in: T.S. Horst Czichos, Leslie Smith (Ed.) Springer handbook
636 of materials measurement methods, Springer Berlin Heidelberg, New York, 2006, pp.
637 371-387
638 [49] H. Borjigin, K.A. Stevens, R. Liu, J.D. Moon, A.T. Shaver, S. Swinnea, B.D.
639 Freeman, J.S. Riffle, J.E. McGrath, Synthesis and characterization of
640 polybenzimidazoles derived from tetraaminodiphenylsulfone for high temperature gas
641 separation membranes, Polymer, 71 (2015) 135-142.
642 [50] R. He, Q. Li, A. Bach, J. Jensen, N. Bjerrum, Physicochemical properties of
643 phosphoric acid doped polybenzimidazole membranes for fuel cells, J. Membr. Sci.,
644 277 (2006) 38-45.
645 [51] X. Glipa, B. Bonnet, B. Mula, D.J. Jones, J. Rozière, Investigation of the
646 conduction properties of phosphoric and sulfuric acid doped polybenzimidazole, J.
647 Mater. Chem., 9 (1999) 3045-3049.
648 [52] S.R. Samms, S. Wasmus, R.F. Savinell, Thermal stability of proton conducting
649 acid doped polybenzimidazole in simulated fuel cell environments, J. Electrochem.
650 Soc., 143 (1996) 1225-1232.
651 [53] S.C. Kumbharkar, P.B. Karadkar, U.K. Kharul, Enhancement of gas permeation
652 properties of polybenzimidazoles by systematic structure architecture, J. Membr. Sci.,

653 286 (2006) 161-169.
654 [54] K.A. Stevens, J.D. Moon, H. Borjigin, R. Liu, R.M. Joseph, J.S. Riffle, B.D.
655 Freeman, Influence of temperature on gas transport properties of
656 tetraaminodiphenylsulfone (TADPS) based polybenzimidazoles, J. Membr. Sci., 593
657 (2020) 117427.
658 [55] S. Luo, J.R. Wiegand, P. Gao, C.M. Doherty, A.J. Hill, R. Guo, Molecular origins
659 of fast and selective gas transport in pentiptycene-containing polyimide membranes and
660 their physical aging behavior, J. Membr. Sci., 518 (2016) 100-109.
661 [56] J.Y. Park, D.R. Paul, Correlation and prediction of gas permeability in glassy
662 polymer membrane materials via a modified free volume based group contribution
663 method, J. Membr. Sci., 125 (1997) 23-39.
664 [57] B.W. Rowe, L.M. Robeson, B.D. Freeman, D.R. Paul, Influence of temperature on
665 the upper bound: Theoretical considerations and comparison with experimental results,
666 J. Membr. Sci., 360 (2010) 58-69.
667 [58] E.J. Moskala, S.E. Howe, P.C. Painter, M.M. Coleman, On the role of
668 intermolecular hydrogen bonding in miscible polymer blends, Macromolecules, 17
669 (1984) 1671-1678.
670 [59] D.J. Skrovanek, S.E. Howe, P.C. Painter, M.M. Coleman, Hydrogen bonding in
671 polymers: Infrared temperature studies of an amorphous polyamide, Macromolecules,
672 18 (1985) 1676-1683.
673 [60] Z. Ali, F. Pacheco, E. Litwiller, Y. Wang, Y. Han, I. Pinnau, Ultra-selective defect-
674 free interfacially polymerized molecular sieve thin-film composite membranes for H_2
675 purification, J. Mater. Chem. A, 6 (2018) 30-35.
676 [61] L.M. Robeson, The upper bound revisited, J. Membr. Sci., 320 (2008) 390-400.
677 [62] Y. Peng, Y. Li, Y. Ban, H. Jin, W. Jiao, X. Liu, W. Yang, Metal-organic framework
678 nanosheets as building blocks for molecular sieving membranes, Science, 346 (2014)
679 1356-1359.
680 [63] Y.-S. Li, F.-Y. Liang, H. Bux, A. Feldhoff, W.-S. Yang, J. Caro, Molecular sieve
681 membrane: Supported metal-organic framework with high hydrogen selectivity, Angew.
682 Chem. Int. Ed., 49 (2010) 548-551.

683 [64] L.F. Villalobos, R. Hilke, F.H. Akhtar, K.-V. Peinemann, fabrication of
684 polybenzimidazole/palladium nanoparticles hollow fiber membranes for hydrogen
685 purification, Adv. Energy Mater., 8 (2018) 1701567.
686 [65] T. Yang, G.M. Shi, T.S. Chung, Symmetric and asymmetric zeolitic imidazolate
687 frameworks (ZIFs)/polybenzimidazole (PBI) nanocomposite membranes for hydrogen
688 purification at high temperatures, Adv. Energy Mater., 2 (2012) 1358-1367.
689 [66] T. Yang, Y. Xiao, T.S. Chung, Poly-/metal-benzimidazole nano-composite
690 membranes for hydrogen purification, Energy Environ. Sci., 4 (2011) 4171-4180.
691 [67] M. Shan, X. Liu, X. Wang, I. Yarulina, B. Seoane, F. Kapteijn, J. Gascon, Facile
692 manufacture of porous organic framework membranes for precombustion CO_2 capture,
693 Sci. Adv., 4 (2018) eaau1698.
694

Graphical Abstract

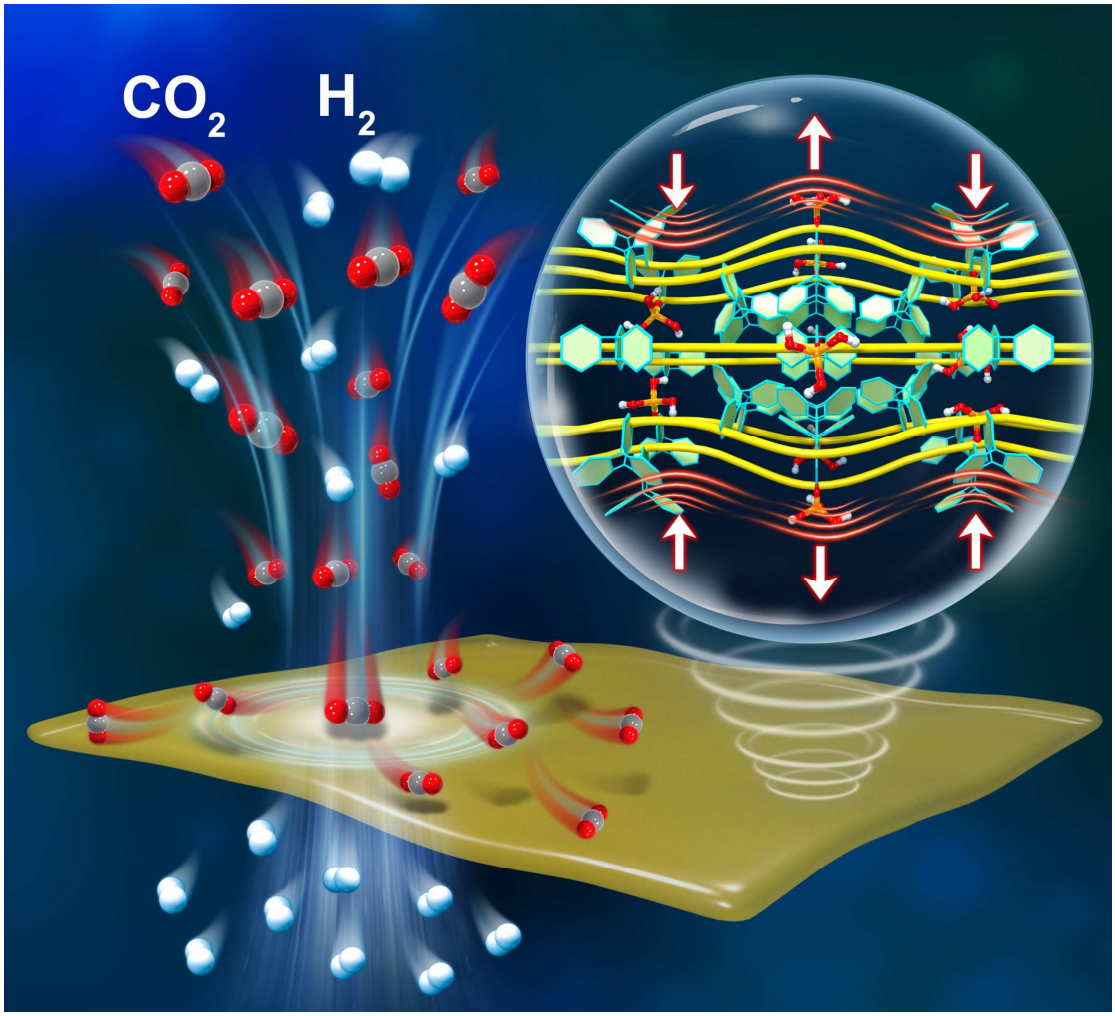

Scheme demonstrating novel macromolecular engineering of polybenzimidazole (PBI) membranes *via* controllable manipulation of microporous architecture. Hierarchical triptycene moieties disrupt chain packing and introduce additional configurational free volumes for high permeability. Phosphoric acid doping enhances molecule sieving *via* hydrogen bonding and proton transfer.